




Article

Flame Spray Pyrolysis Co₃O₄/CoO as Highly-Efficient Nanocatalyst for Oxygen Reduction Reaction

Loukas Belles ¹, Constantinos Moularas ¹, Szymon Smykała ²  and Yiannis Deligiannakis ^{1,*}

¹ Laboratory of Physics Chemistry of Materials & Environment, Department of Physics, University of Ioannina, 45550 Ioannina, Greece; loukasbelles@gmail.com (L.B.); k.moularas@uoi.gr (C.M.)

² Institute of Engineering Materials and Biomaterials, Silesian University of Technology, 18a Konarskiego St, 44-100 Gliwice, Poland; szymon.smykala@polsl.pl

* Correspondence: ideligia@uoi.gr

Abstract: The oxygen reduction reaction (ORR) is the rate-limiting reaction in the cathode side of fuel cells. In the quest for alternatives to Pt-electrodes as cathodes in ORR, appropriate transition metal oxide-based electrocatalysts are needed. In the present work, we have synthesized Co₃O₄ and CoO/Co₃O₄ nanostructures using flame spray pyrolysis (FSP), as electrocatalysts for ORR in acidic and alkaline media. A detailed study of the effect of (Co-oxide)/Pt ratio on ORR efficiency shows that the present FSP-made Co-oxides are able to perform ORR at very low-Pt loading, 0.4% of total metal content. In acid medium, an electrode with (5.2% Pt + 4.8% Co₃O₄), achieved the highest ORR performance ($J_{\max} = 8.31 \text{ mA/cm}^2$, $E_{1/2} = 0.66 \text{ V}$). In alkaline medium, superior performance and stability have been achieved by an electrode with (0.4%Pt + 9.6% (CoO/Co₃O₄)) with ORR activity ($J_{\max} = 3.5 \text{ mA/cm}^2$, $E_{1/2} = 0.08 \text{ V}$). Using XRD, XPS, Raman and TEM data, we discuss the structural and electronic aspects of the FSP-made Co-oxide catalysts in relation to the ORR performance. Cyclic voltammetry data indicate that the ORR process involves active sites associated with Co³⁺ cations at the cobalt oxide surface. Technology-wise, the present work demonstrates that the developed FSP-protocols, constitutes a novel scalable process for production of co-oxides appropriate for oxygen reduction reaction electrodes.

Keywords: Oxygen Reduction Reaction (ORR); Flame Spray Pyrolysis (FSP); cobalt oxide; nanomaterials; fuel cells; rotating disc electrode (RDE)



Citation: Belles, L.; Moularas, C.; Smykała, S.; Deligiannakis, Y. Flame Spray Pyrolysis Co₃O₄/CoO as Highly-Efficient Nanocatalyst for Oxygen Reduction Reaction. *Nanomaterials* **2021**, *11*, 925. <https://doi.org/10.3390/nano11040925>

Academic Editor: Shiqiang (Rob) Hui

Received: 24 February 2021

Accepted: 1 April 2021

Published: 5 April 2021

Publisher's Note: MDPI stays neutral with regard to jurisdictional claims in published maps and institutional affiliations.



Copyright: © 2021 by the authors. Licensee MDPI, Basel, Switzerland. This article is an open access article distributed under the terms and conditions of the Creative Commons Attribution (CC BY) license (<https://creativecommons.org/licenses/by/4.0/>).

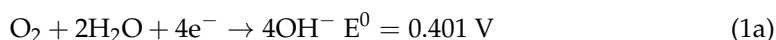
1. Introduction

Flame spray pyrolysis (FSP) is an established versatile one-step process for scalable synthesis of metal-oxide nanocrystals, with precisely controlled properties [1]. During the last two decades, FSP technology has been explored for synthesis of various types of nanomaterials e.g., metal-oxides, metallic particles, and heterojunctions [2,3] to name a few. Control of the combustion-flame characteristics, i.e., reactor configuration, reactants composition, temperature profiles, allow control of particle composition [4,5], size [4,5], morphology [5,6], defects [3]. These factors are known to be crucial for optimal catalytic or electrocatalytic performance [7,8].

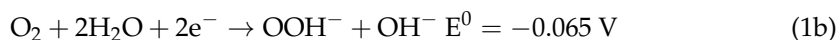
In fuel cells cathodes, the one-electron reduction of O₂ to form OO[−] (ORR) is thermodynamically non-favorable [9]. As a result, the ORR process is not spontaneous, therefore an appropriate catalyst is mandatory, which usually requires a non-zero voltage bias [7,10]. Usually, ORR can proceed via two well-known pathways, i.e., either two-, or four-electrons pathway [11]. The preferable path strongly depends on factors such as pH of the electrolyte [12], operation temperature [13], and mostly on the type of catalytic material [4,7,11,14]. Equation (1a–f) summarize the pertinent electron transfer reactions [15,16] for Pt⁰ which is the benchmark material in ORR research [17,18], at acidic or alkaline pH respectively [9,12].

1.1. Alkaline Medium

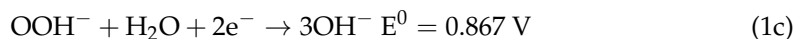
Direct Pathway (4 e⁻ process)



Sequential Pathway-Step a (2 e⁻ process):

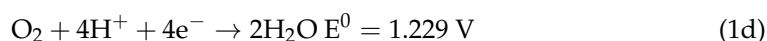


Sequential Pathway-Step b (2 e⁻ process):

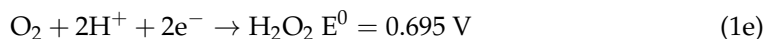


1.2. Acidic Medium

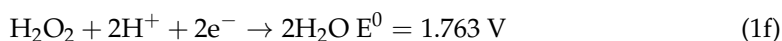
Direct Pathway (4 e⁻ process)



Sequential Pathway-Step a (2 e⁻ process)



Sequential Pathway-Step b (2 e⁻ process)



When the overall efficiency of a fuel-cell is considered, the two-electron pathway usually results to lower efficiency than the four-electron, therefore typically the 4 e⁻ pathway is desired to achieve high-efficiency in fuel cells [9]. As described in Equation (1), the electron-transfer reaction pathways can be either direct or sequential [19], i.e., the sequential pathway is not a necessary intermediate for the direct pathway. At acidic-medium in the sequential-reaction scheme, the formation of hydrogen peroxide, H₂O₂, intervenes Equation (1e,f). This is non-desirable, thus the sequential-process in acid-medium should be suppressed [8,19]. In alkaline medium, the key-intermediate is an OOH⁻ anion, Equation (1b,c). The rate-limiting steps in ORR can be determined by [a] the adsorption-events of O₂ or OOH_(ads) [20] in acid or alkaline medium, or [b] the desorption of the formed hydroxyl-anions OH⁻, that can be in the form of H₂O (i.e., H⁺ + OH at acidic medium) or OH⁻ (alkaline medium) [21]. According to He and Cairns [9], the overpotential required for ORR is correlated with the difference of equilibrium potential between the {first electron transfer} and {overall reaction}. Thus, eligible catalysts for ORR should cope with all these rate-limiting factors, in addition they should poses appropriate stability.

Today, state-of-the-art ORR cathodes are made by noble metals like platinum [11], palladium [22], their alloys [23], or bimetallic catalysts [24]. Typically, the best-performing catalytic noble metals are nanosized, usually supported on an appropriate conductive carbon-support [25,26]. So far, platinum/carbon (Pt⁰/C) cathodes are the most promising candidates for ORR, in both alkaline and acidic media [27], due to their good electrocatalytic activity [28] and stability [29]. However, the high-cost and environmental scarcity of Pt are prohibitive factors, thus, low-cost/earth-abundant metal oxide catalysts are at immediate need. Moreover, the properties of the carbon-support, i.e., such as graphitization quality, conductivity, O₂ diffusion and surface area affect the ORR activity and catalyst's durability. So far, only few eligible non-noble metals have been reported, i.e., most reported cases display inferior ORR performance vs. Pt [30,31]. An alternative strategy is to develop alloys of Pt with inexpensive metals e.g., Ni, Co, Cu, or Fe [30]. The premise of this approach is that, if efficient ORR can be achieved, this could be combined with improvement of the stability of the Pt cathode, since Pt suffers from dissolution or agglomeration [15]. In this

direction, {noble/non-noble metal} alloys have been extensively studied as ORR cathodes in acidic media [31].

Recently, encouraging results on non-noble metal-oxides have been reported for ORR cathodes [32]. Theoretical and experimental studies of some transition metal oxides (TMOs) [19], i.e., cobalt oxides [33], copper oxides [34], manganese oxides [35] and iron oxides [36], Some mixed transition metal oxides, i.e., $\text{ZnCo}_2\text{O}_4/\text{C}$ [37], CoCuMnO_x [38], CoO/MnO_2 [39] show encouraging results on ORR efficiency [40], while a study on $\text{Co}_x\text{Si}_y\text{O}_z$ reported a highly satisfactory stability [41]. Among TMOs, cobalt-oxide is a promising candidate, thanks to its low price, with ability to be stabilize $\text{Co}^{3+}/\text{Co}^{2+}$ oxidation-states [42]. More particularly Co_3O_4 is a spinel-type $\{2\text{Co}^{3+}-1\text{Co}^{2+}\}$ structure, where Co^{3+} -cations occupy octahedral sites and Co^{2+} -cations occupy tetrahedral sites [43], see inset in Figure 1B. In principle, the occurrence of the $\text{Co}^{2+}/\text{Co}^{3+}$ redox couple in the Co_3O_4 unit-cell, provides an option for electron transfer [43]. In this context, cobalt-oxide nanoparticles supported on graphene [30] or carbon nanotubes [44] have been reported as efficient ORR cathode electrodes. However, their performance was satisfactory only in alkaline medium, not in acidic medium [19,45]. The issue of efficient ORR operation at both acidic and alkaline medium remains a cumbersome challenge [19,46] that requires diligent control of interfacial adsorption-desorption of O-species/electrons and protons [46].

In this context, specific aims of the present work were: (1) using FSP-technology to synthesize Co-oxide nanomaterials optimized for ORR at both acidic and alkaline environment, (2) to construct efficient ORR electrodes with very-low Pt-content, operating at both alkaline and acid medium, and (3) to investigate the role of nanoparticle properties, with specific emphasis on phase composition ($\text{Co}_3\text{O}_4/\text{CoO}$) and $\text{Co}^{2+}/\text{Co}^{3+}$ redox speciation.

2. Materials and Methods

Chloroplatinic acid hexahydrate ($\text{H}_2\text{PtCl}_6 \cdot 6\text{H}_2\text{O}$, Sigma-Aldrich, (Saint Louis, MO, USA), Sodium Borohydride (NaBH_4), used to form the Pt nanoparticles were purchased from Sigma Aldrich (Saint Louis, MO, USA). Carbon black (Vulcan XC-72R) was a kind-gift from Cabot (Boston, MA, USA), was used as-received as the support of the electrocatalysts.

2.1. Synthesis of Co-Based Nanocatalysts by Flame Spray Pyrolysis

Our lab-scale FSP reactor, used to produce the Co-oxides, has been described in detail previously [6,46]. To prepare Co_3O_4 , a 0.3 M Co-precursor solution was prepared by dissolving cobalt acetate in a mixture of solvents consisting of 50% acetic acid, 40% iso-octane, 10% 2-butanol. In FSP-process, the high combustion enthalpy of iso-octane (5460 kJ/mol) increases the high temperature regime and flame length, thus promoting the desired gas-to-particle formation [3]. The precursor fuel (P) was supplied to the nozzle through a syringe pump at a feed rate of 5 mL/min and atomized into fine droplets, using a dispersion oxygen (D) flow of 5 L/min, i.e., $P/D = 5/5$, at a pressure-drop of 1.5 bar. The spray-ignition was initiated and sustained by a surrounding, supporting flamelet ring of premixed O_2/CH_4 (3/1.5 L/min). The $\text{CoO}/\text{Co}_3\text{O}_4$ heterostructure was produced by increasing the fuel in the flame to $P = 8$ mL/min. This {precursor to dispersion} ratio $P/D = 8/5$, resulted in a slightly O-lean flame, i.e., $\phi = 0.9$ thus promoting the suboxic CoO phase [47]. The flame flow-directionality was assisted by an additional 5 L/min sheath O_2 , provided thorough a toroidal-ring with 16 holes, 500 μm diameter each, located annularly at 2 cm around the nozzle tip. A vacuum pump (Busch V40) was used to collect the particles on a glass microfiber filter (Albeit), at a Burner-to-Filter Distance BFD = 60 cm, above the flame. The product powder was collected from the filter by scraping. The so prepared Co-oxide materials are herein codenamed as #Co1, #Co2, and #Co3 for the as-prepared Co_3O_4 , the calcined (500 °C, 8 h), and the $\text{Co}_3\text{O}_4/\text{CoO}$ material, repressively, see Table 1.

Table 1. Structural characterization data for the FSP-made Co.oxide nanomaterials.

Material	d_{BET} (nm ± 0.5)	d_{XRD} (nm ± 0.5)	d_{TEM} (nm ± 2)	SSA (m ² g ⁻¹ ± 5)	wt% Co ₃ O ₄ (±5%)	wt% CoO (±5%)	Co ²⁺ /Co ³⁺ *	O_{ads}/O_{latt} *
Pt/C	3.5	4	-	100	-	-	-	-
Co#1	10	10	11	100	100	0	0.52	0.53
Co#2	32	27	37	30	100	0	0.48	1.3
Co#3	53	11(Co ₃ O ₄) 9(CoO)	44	18	66	34	0.71	0.58

* derived from XPS measurements.

2.2. Characterization of Nanocatalysts

X-Ray Diffraction (XRD): The crystal structures of the nanocatalysts were analyzed by XRD in a Bruker Advance D8 diffractometer (Cu K α radiation $\lambda = 1.5406 \text{ \AA}$, 40 kV, 40 mA) at $2\theta = 10^\circ\text{--}80^\circ$ (step size of 0.03° at a rate of 2 s per step). The average crystallite size of FSP-made particles was calculated by the Scherrer equation [48]

$$d_{XRD} = \frac{k\lambda}{\beta(\cos\theta)} \quad (2)$$

where d_{XRD} is the crystallite size (nm), k is a shape constant (in this case 0.9), λ is the wavelength of Cu K α radiation (1.5406 \AA), β is the full width at half maximum and θ is the peak-diffraction angle.

Brunauer–Emmett–Teller (BET) Analysis: The specific-surface-area (SSA, m²/gr) of the synthesized materials was determined by the N₂ adsorption-desorption method [49] at 77 K using a Quantachrome Autosorb-1 instrument (Bounton Beach, FL, USA). To acquire the BET isotherms, powders were degassed for 2 h at 120 °C, in flowing N₂ over a relative pressure range of $P/P_0 = 0\text{--}1$. An average primary particle size, d_{BET} , was calculated by the estimated SSA assuming monodisperse spheres according to the Equation (3) [50]

$$d_{BET} = \frac{6}{\rho_p \cdot SSA} \quad (3)$$

where ρ_p is the weighted density of the particles with $\rho [\text{Co}_3\text{O}_4] = 5.18 \text{ g/cm}^3$ and $\rho [\text{CoO}] = 6.44 \text{ g/cm}^3$ [51].

X-Ray Fluorescence (XRF): Sample excitation was performed with an annular 109 Cd radio-isotopic source (RITVERC GmbH). X-ray source had a radius of 12.5 mm housed in a cylindrical container, fixed coaxially above a CANBERRA SL80175 Si(Li) detector (5 mm crystal thickness, 80 mm² area), with a 25 μm -thick Be window and an energy resolution of 171 eV for the 5.9 keV Mn K α line. Data acquisition was performed using a PCI card, controlled by the ORTEC MAESTRO–32 software, and spectral analysis was carried out using the WinQxas software package (International Atomic Energy Agency Laboratories Seibersdorf, XRF Group, Seibersdorf (Austria), IAEA 1997–2002).

Raman Spectroscopy: Raman spectroscopy measurements were performed with a HORIBA XploRA PLUS instrument (Kyoto, Japan) with a 785 nm diode laser as excitation source, focused with a microscope. The materials were pressed into pellets and placed on a glass plate. Each Raman spectrum was recorded performing 30 accumulations in 10 s, to obtain adequate signal-to-noise ratio.

TEM: The morphology of the materials was analyzed by transmission electron microscopy using a FEI Titan 80–300 S/TEM microscope at 300 kV accelerating voltage and a 21.5 mrad beam convergence angle. Before the measurements, the nanopowders were dispersed in ethanol, sonicated at a bath sonicator and then deposited as single droplet of suspension on a copper TEM grid covered with a thin carbon layer. Selected area electron diffraction patterns were acquired with the same instrument in TEM mode, under parallel electron beam illumination.

X-Ray Photoelectron Spectroscopy (XPS) data were acquired in a surface analysis ultrahigh vacuum system (SPECS GmbH) equipped with a twin Al-Mg anode X-ray source and a multichannel hemispherical sector electron analyzer (HSA-Phoibos 100). The base pressure was $2\text{--}5 \times 10^{-9}$ mbar. A monochromatized Mg K α line at 1253.6 eV and an analyzer pass-energy of 15 eV were used in all measurements. The binding energies were calculated with reference to the energy of C1 s peak of adventitious carbon at 284.5 eV. The peak deconvolution was calculated using CasaXPS software with a Shirley background.

2.3. Preparation of Electrocatalytic Working Electrodes

Pt⁰-particles were synthesized as a reference catalyst, employing the wet-impregnation method [52], based on formation of fine Pt⁰ particles via reduction of Pt²⁺ by BH₄⁻. Briefly, 85 mg of the Pt-salt was dissolved in 8 mL of ultra-pure triple distilled water (Millipore SIMS600 CP Burlington, USA) at room temperature, T = 23 °C, plus 320 mg of Vulcan XC-72 R carbon black. The mixture was allowed to mix under continuous stirring for 2 h, until it became a homogeneous black slurry. Then, NaBH₄ was added dropwise to the Pt/carbon slurry, using a 10 μ L pipet, at a rate of 1 mL/min under vigorous stirring. The NaBH₄ was taken from a stock of 31 mg NaBH₄ dissolved in 8 mL of triple distilled water. The reduction potential of the NaBH₄/Pt/carbon slurry was E_h = -65 mV vs. NHE, Ref. [53] monitored in-situ by a redox Pt-electrode (Metrohm, Pt Working Electrode 3 mm diameter Herisau, Switzerland). Then, the resulting NaBH₄ /Pt/carbon slurry was heated under stirring for 12 h at 90 °C, and afterwards the formed solid residue was collected by centrifugation at 6000 rpm. The collected solid was dried for 5 h at 23 °C under a N₂ stream. This material, herein codenamed as {10 wt% Pt/C}, had a Pt-loading of 10.1% as determined by XRF.

The electrocatalytic materials were deposited as drop-casted films, on a glassy-carbon disk electrode (working electrode RDE.GC30 by Metrohm Autolab B.V.), with a 3 mm diameter (with a geometric surface area of 0.071 cm²), mounted on a RDE holder (RDE-2 Metrohm Autolab B.V.). To construct the electrode, first a catalyst-suspension was prepared containing 7 mg of the material-powder in 6 mL mixture of triple distilled water (2.75 mL) and isopropanol (3.25 mL) (Merck, ACS Reag, NJ, USA) [29]. Depending on the experiment, the catalyst-powder was either Pt⁰-particles, or FSP-made Co-oxide particles, or appropriate mixtures of {Pt⁰-particles/plus FSP-made Co-oxide particles}.

Before the drop-casting step, the catalyst mixture was ultrasonicated using a 20 W ultrasonication bath (Elmasonic S10 h, Singen, Germany) to achieve a homogeneous slurry [54]. Deposition of each electrocatalyst material on the working disk-electrode was performed by drop-casting of the prepared suspension onto the glassy-carbon disk. Before drop-casting each glassy electrode was polished with aluminium oxide powder (grain size 0.3 μ m) on a polishing cloth, as recommended by Metrohm. Then, 25 μ L of the catalyst suspension was drop-casted on to the glassy carbon, using a micro-pipette (1 μ L per drop), and rapidly dried at room temperature 23 °C, forming a dry {catalyst/carbon} film on the glassy-carbon. Then, 3 μ L of Nafion-solution was drop-casted on the formed film and allowed to dry at room temperature 23 °C, forming a dry {Nafion:catalyst/carbon} film on the glassy-carbon. The Nafion-solution consisted of 5 wt% perfluorinated Nafion resin solution (Sigma Aldrich, MO, USA), in triple distilled water/isopropanol (110 μ L Nafion solution: 5.5 mL triple distilled water: 6.5 mL isopropanol). According to the standard procedure, the deposition of a Nafion on top of the catalyst film acts as a binding agent [55] stabilizing the electrode.

2.4. Catalytic ORR Evaluation

All ORR experiments were carried out at room temperature, 23 °C, in a three-compartment-cell, filled with 50 mL triple distilled water containing either 0.1 M H₂SO₄ for acidic media measurements or 0.1 M NaOH for alkaline media measurements. An Ag/AgCl (3 M KCl) electrode (Metrohm A.G.) was used as reference electrode and a Pt-wire electrode as

counter-electrode. All the potential values were calculated versus Ag/AgCl, using the reference value + 0.21 V versus SHE at 20 °C [56].

To evaluate the ORR catalytic activity of our nanomaterials, we used the {Nafion:catalyst/carbon} glassy carbon electrode, mounted on the rotating-disk electrode (RDE) set-up. To evaluate the ORR kinetics, different rotation speeds were tested from 500 up to 3000 rpm of the RDE. The ORR measurements in acid conditions, were done in a O₂-saturated cell containing 50 mL of triple distilled water, 0.1 M H₂SO₄ (pH = 1.3). At each rotation speed, ORR currents were measured versus the applied bias DC-potential, that was scanned linearly in the range E_{bias} = −0.2 V to +1 V, vs. Ag/AgCl, at a scan-speed of 10 mV/s. The ORR measurements in alkaline conditions were made in a O₂-saturated cell, in 50 mL of triple distilled water, containing 0.1 M NaOH (pH = 13.4). At each rotation speed, ORR currents were measured versus the applied bias DC-potential that was varied linearly in the range of E_{bias} = −0.4 V to +0.4 V, versus Ag/AgCl, at a scan-speed of 10 mV/s. ORR polarization curves were recorded as Y = current density (J) vs. X = applied potential, where J was normalized as per geometric surface of the electrode, i.e., typically 0.071 cm². According to the standard ORR procedures [31] the total mass (catalyst and carbon-support) per surface area was adjusted at 0.41 mg per cm², allowing uninhibited conductivity between the glassy carbon and the active-phases, as well as proper signal-to noise [55]. Thus, in all our experiments discussed herein, the amount of the metal catalyst was 3 µg, accounting for 10% of the total {Nafion:catalyst/carbon} mass amount. Each electrochemical run was repeated for 50 repetitive cycle-scans.

Data analysis: The half-wave potential E_{1/2} is defined as the potential at which the measured current equals half the limiting current. Typically, E_{1/2} is used in ORR studies as a measure of the electrocatalytic activity, i.e., more positive E_{1/2} value, for the same rotation speed of the RDE, indicates a higher ORR activity [8,55,57]. In a given ORR data-set, recording J at various electrode rotation speeds (ω) provides data that, when analyzed according to Koutechy–Levich [54,55], provide information on the underlying electron-transfer characteristics of the ORR process [55]. The Koutechy–Levich equations are

$$\frac{1}{J_{lim}} = \frac{1}{J_k} + \frac{1}{J_l} = \frac{1}{J_k} + \frac{1}{B\omega^{1/2}} \quad (4)$$

$$B = 0.62 n F D^{2/3} \nu^{-1/6} C_b \quad (5)$$

$$J_k = nFkC_b \quad (6)$$

In Equation (4) J_{lim} is the measured (limiting) current density in (mA/cm²), J_k and J_L are the kinetic- and diffusion- limiting current densities [43], and ω the rotation frequency of the RDE (in rpm). The kinetic current, J_k is defined as the current that would be observed in the absence of mass-transport limitations, was calculated using Equation (4) from a plot of J_{lim} vs. (1/ω^{1/2}). F is Faraday's constant (96485 C mol^{−1}), D is the oxygen diffusion coefficient (1.9 × 10^{−5} cm² s^{−1}) [43], ν is the kinematic viscosity of the electrolyte that is (0.01 cm² s^{−1}) for 0.1 M NaOH and (0.03 cm² s^{−1}) for 0.1 M H₂SO₄ [43,58], C_b is the bulk concentration of oxygen (1.2 × 10^{−6} mol cm^{−3}) [43], and k is the electron-transfer rate constant [43]. The integer n is the number of electrons transferred per reduced O₂ molecule, that can be estimated using Equation (6) [43]. Notice that, it is the value of n, i.e., 2 or 4, that discriminates a two- or four-electron ORR process, as described in Equation (1).

3. Results

3.1. Characterization of the FSP-Made Cobalt-Oxide Nanocatalysts

Figure 1A shows XRD patterns for the #Co1, #Co2, and #Co3 materials. For #Co1, #Co2 the characteristic diffraction peaks at angles 19.1°, 31.3°, 36.8°, 38.8°, 44.6°, 55.8°, 59.5°, and 65.3° can be perfectly indexed to the (111), (220), (311), (222), (400), (422), (511), and (440) planes of Co₃O₄ (JCPDS card no. 75–2480) respectively [59]. For #Co3, additional characteristic peaks at 36.7°, 42.64°, 61.71°, 74.03°, and 77.98° can be indexed to the (111), (200), (220), (311) and (222) planes of CoO (JCPDS card no. 14–0133) respectively [60],

indicating the phase composition of #Co3 was $\text{Co}_3\text{O}_4/\text{CoO}$. The CoO-phase was formed by Co^{2+} atoms, i.e., reduced Co^{3+} , formed in-situ in FSP under our specific combustion conditions. Specifically, we have adjusted the fuel-to-oxygen equivalence ratio at $\varphi = 0.9$, which corresponds to an oxygen-lean combustion process, promoting the stabilization of reduced Co^{2+} and thus the CoO crystal formation, see Table 1. In the case of #Co1 material, the fuel-to-oxygen equivalence ratio was adjusted to $\varphi = 0.7$ which is oxygen-rich, thus no CoO-phase formation was observed, only Co_3O_4 phase was formed. In this way, adjustment of the combustion process parameters in FSP allowed a fine control of the Co_3O_4 & CoO nanophases. To examine the effect of a mild post-FSP calcination, i.e., that typically improves crystallinity in nanoparticles, a post-FSP calcination of #Co1 at $T = 500^\circ\text{C}$ for 180 min was applied. As expected, calcination increased the primary particle size, i.e., d_{XRD} was increased from 10 nm in #Co1, to 27 nm in #Co2, with a concomitant decrease of the SSA from $100\text{ m}^2/\text{gr}$ to $30\text{ m}^2/\text{gr}$, see Table 1.

Representative TEM images, depicted in Figure 1B–D, show high-quality crystal planes formation in the FSP-made materials #Co1 and #Co3 as well as in #Co2. Macroscopically, the nanoparticles were associated in fractal-like morphologies, typical for FSP-made metal-oxide particles [46]. Figure 1B–D show well-resolved lattice-fringes with d-spacing 0.28 nm, assigned to the (220) Miller-planes of Co_3O_4 phase in #Co1, #Co2 and #Co3 respectively [61]. In #Co3, the lattice-fringes with d-spacing 0.23 nm, in Figure 1D, are attributed to CoO crystal [62]. The particle size distribution, Figure 1E–G, show that #Co1 consisted of particles size in a range of 7–16 nm, with an average diameter $d_{\text{TEM}} = 10.5\text{ nm}$, #Co2 had a wider range of particles size 20–60 nm with an average $d_{\text{TEM}} = 35.5\text{ nm}$ and #Co3 which had a wider range of particles size 29–60 nm with an average $d_{\text{TEM}} = 45\text{ nm}$. Interestingly, in #Co2, i.e., calcined #Co1, the d_{XRD} diameter, is smaller than the BET- or TEM-derived particle size, per Table 1. This is a nice demonstration that d_{XRD} diameter is determined from the size of the primary crystalline size, while particle-sintering and agglomeration phenomena influence the BET and TEM derived particle size. An analogous observation holds true for the #Co3 material.

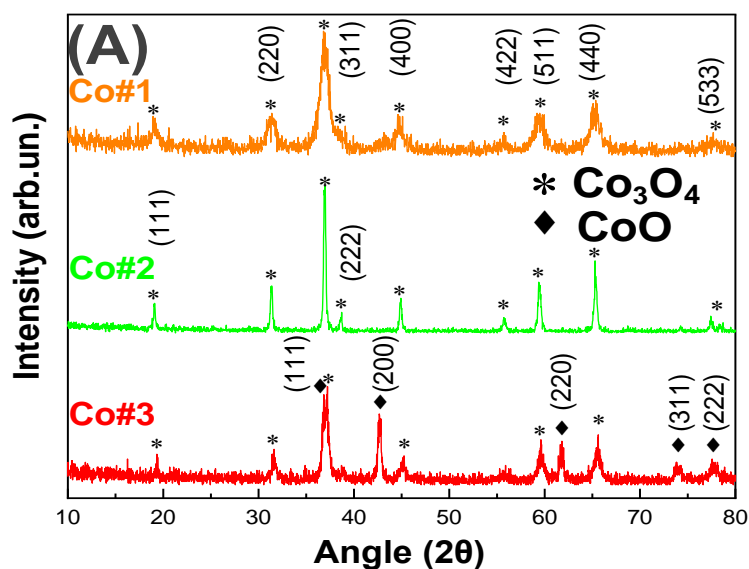


Figure 1. Cont.

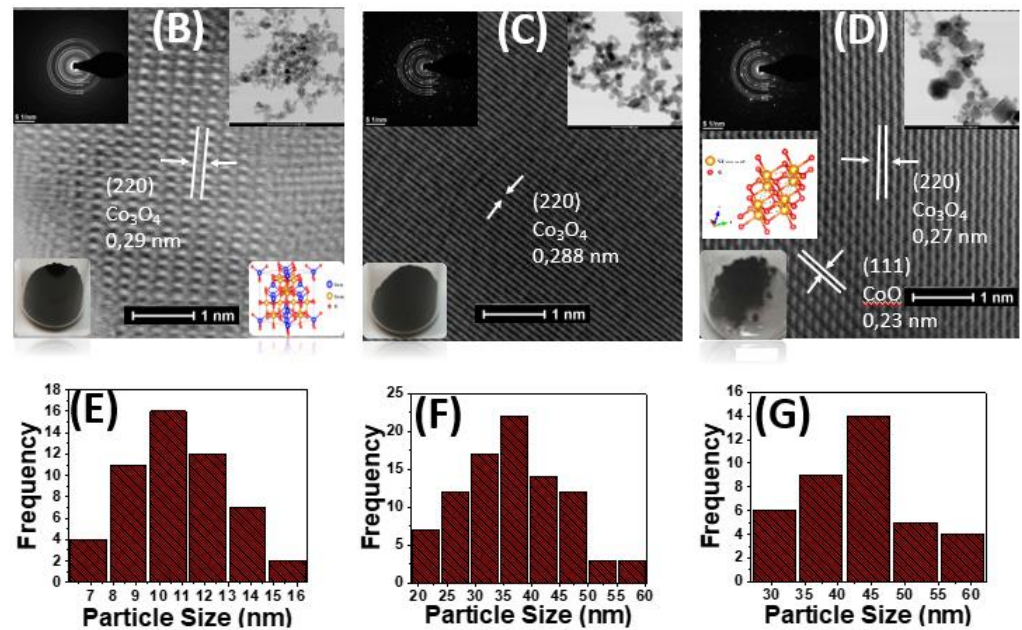


Figure 1. TEM images and (A) XRD pattern of our #Co1, #Co2 and #Co3 nanomaterials. (B) As prepared Co₃O₄, #Co1, (C) Calcined Co₃O₄, #Co2 and (D) CoO@Co₃O₄ particles #Co3. Insets: SAED pattern of #Co1, #Co2 #Co3 respectively and photos of the powders. Size pattern distribution histograms of (E) #Co1 (F) #Co2 (G) #Co3.

Raman Spectroscopy: Figure 2 illustrates Raman spectra for the FSP-made Co-oxide nanomaterials. In all Raman spectra the characteristic vibration peaks of Co₃O₄ are prominent [60]. Specifically, the peaks at 189.5 cm⁻¹, 471.3 cm⁻¹, 516 cm⁻¹, 610 cm⁻¹, and 680 cm⁻¹ in the spectra of #Co1 and #Co2 are assigned to the asymmetric- and bending-vibrations of Co₃O₄ spinel [63]. Upon calcination of #Co1, the improved crystallinity of #Co2 is manifested as sharpened Raman peaks, plus some shifts on peaks at 480 cm⁻¹ and 680 cm⁻¹ band, i.e., compare #Co1 vs. #Co2.

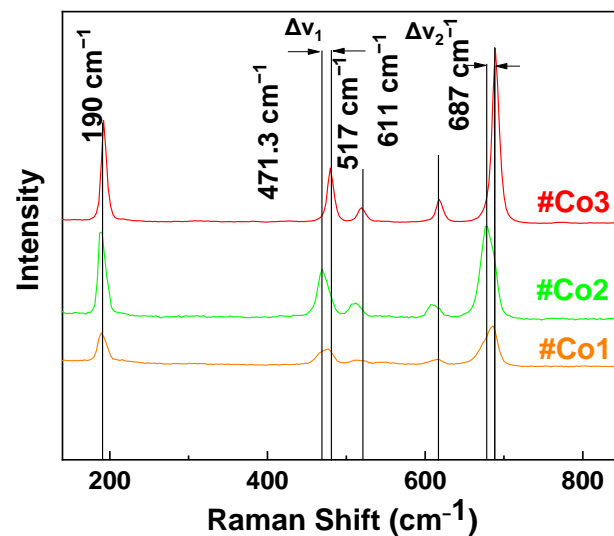


Figure 2. Raman spectra of the FSP-made Cobalt Oxide nanocatalysts.

Material #Co3 displayed distinct Raman peaks at 471.3 cm⁻¹, 517 cm⁻¹, 611 cm⁻¹ and 687 cm⁻¹, in accordance with a mixed-phase CoO/Co₃O₄ [60]. Notice that, the Raman peaks due to CoO are dominating the Raman spectrum of #Co3, despite the lower CoO percentage, i.e., estimated ratio CoO/Co₃O₄ is 34/66 according to XRD. Since the Raman

scattering modes of CoO and Co₃O₄ are not expected to have fundamentally different intensity [60] we consider that the enhanced intensity of CoO in the Raman data in Figure 2, provides an indication of a core-shell configuration where CoO is the shell and Co₃O₄ is the core. Notice that the TEM images in Figure 1, despite their high resolution, do not allow a confirmative detection of core-shell structures, due to the very similar spacing of the Miller planes of CoO and Co₃O₄.

X-Ray Photoelectron Spectroscopy: XPS spectra, presented in Figure 3A–C, were recorded to probe the cobalt oxidation states and the associated oxygen vacancies. In accordance with literature XPS data [64,65], the Co2p_{3/2} and Co2p_{1/2} peaks are detected in Figure 3A–C, with the expected spin-orbit splitting $\Delta E = 15$ eV. The peaks at 779.7 and 781.6 eV are assigned to Co³⁺ and Co²⁺ species respectively [64], as well as the peaks at 794.8 and 796.8 eV [64]. In the case of #Co3 material, the Co²⁺/Co³⁺ ratio was increased (see Table 1), indicating the presence of surface-related defects and/or tetrahedrally-coordinated Co²⁺ species. In order to clarify the origin of Co²⁺ presence, the XPS spectra for O1s have been examined as well, see Figure 3D–F.

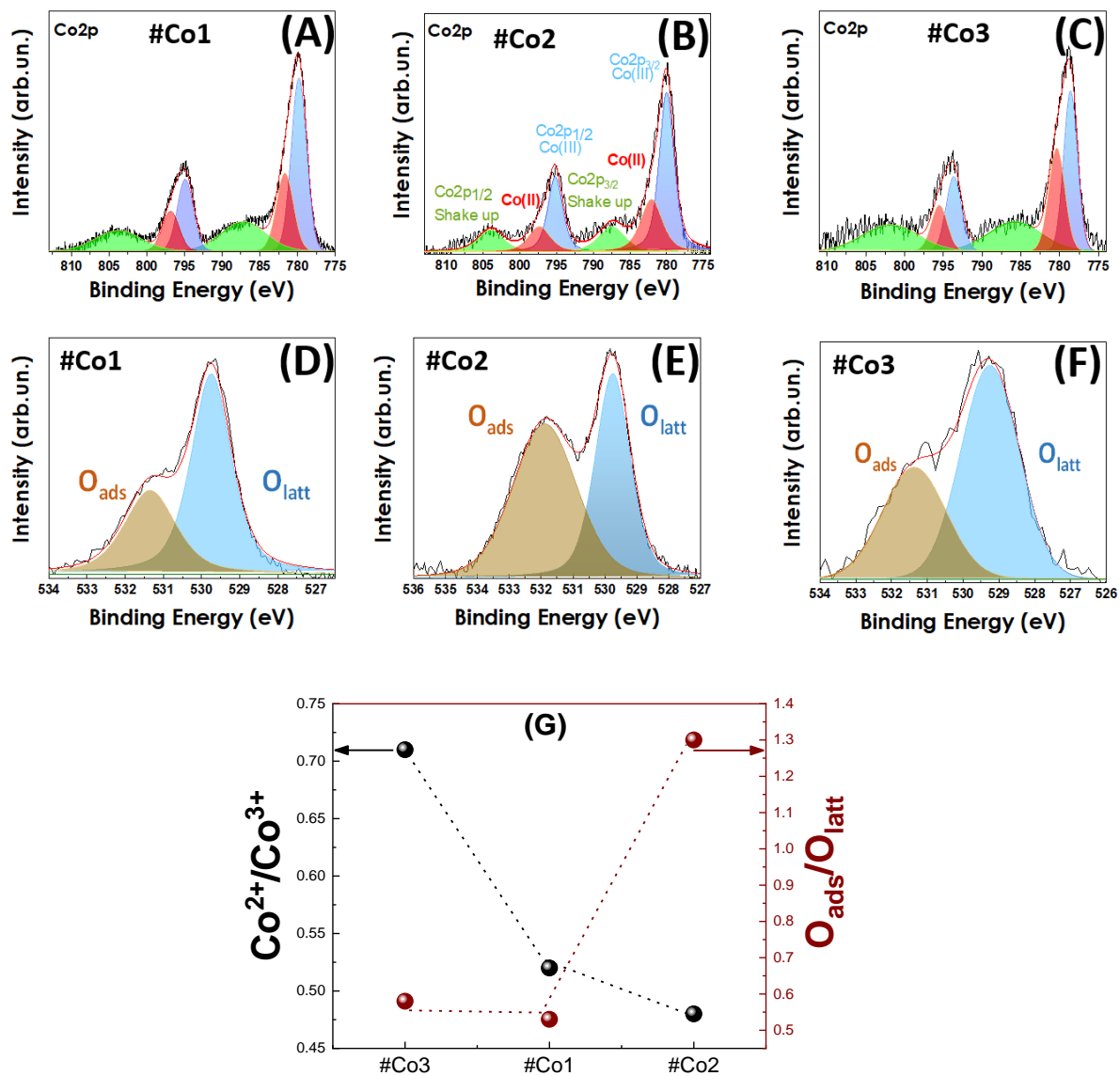


Figure 3. XPS spectra of (A,D) #Co1, (B,E) post-FSP treated #Co2, (C,F) #Co3 XPS for core level of Co2p_{1/2} and Co2p_{3/2} (A–C) and (D–F) for the core level of O1s. (G) the Co²⁺/Co³⁺ ratio, left Y-axis, and O_{ads}/O_{latt} ratio, right Y-axis, for the Co-oxide nanomaterials.

The dominant O-XPS peaks at 529.7 (blue) and 531.3 eV (brown) in Figure 3D–F, correspond to lattice-oxygen and adsorbed-oxygen species respectively [64,65]. As expected, the increased population of surface vacancies in #Co3 material promotes the Co^{2+} states, i.e., compare with #Co1 data in Figure 3D–F. In the case of post-FSP calcined #Co2 material, the increased percentage of adsorbed oxygen is correlated to the expected Co^{3+} formation during annealing. Figure 3G shows a correlation plot for the $\text{Co}^{2+}/\text{Co}^{3+}$ ratio, and $\text{O}_{\text{ads}}/\text{O}_{\text{lattice}}$ ratio, derived from the XPS data. Considering that the formal $\text{Co}^{2+}/\text{Co}^{3+}$ ratio for Co_3O_4 should be $1/2 = 0.5$, i.e., each unit cell contains one Co^{2+} atom and two Co^{3+} atoms, the data in Figure 3G indicate a $\text{Co}^{2+}/\text{Co}^{3+}$ ratio of 0.52 for #Co1 and 0.48 for #Co2, i.e., both are close to 0.5 that is in agreement with the pure Co_3O_4 . In an analogous-manner, material #Co3 with 34% CoO that is nominally consisting of 100% Co^{2+} centers, should have a formal $\text{Co}^{2+}/\text{Co}^{3+}$ ratio of $0.66 \times (0.5) + 0.34 = 0.67$. The data in Figure 3G verify this, i.e., #Co3 had a $\text{Co}^{2+}/\text{Co}^{3+}$ ratio 71%. Taking into account uncertainties in the phase-composition, i.e., by 5%, we consider that the $\text{Co}^{2+}/\text{Co}^{3+}$ ratio determined by XPS is in agreement with the phase-composition $\text{Co}_3\text{O}_4/\text{CoO} \sim 2/1$ from XRD. Thus FSP-technology allows a precise control of phase-composition as well as $\text{Co}^{2+}/\text{Co}^{3+}$ ratio in $\text{Co}_3\text{O}_4/\text{CoO}$ nanomaterials.

3.2. ORR Catalytic Results

3.2.1. Oxygen Reduction Reaction

(1) ORR at Acidic pH: In Figure 4B–D, we present ORR data at acid pH for three working electrodes constructed using the Co-based materials. ORR data for the reference Pt-based electrode, are presented in Figure 4A. In all cases the total-metal loading of each electrode was 10%. In Figure 4B–D the electrode contained {4.8%Co-oxide+5.2% Pt}, i.e., almost half of the Pt mass vs. the reference Pt-based electrode. According to Figure 4B–D all our Co-based electrodes showed the same positive ORR half-wave potential (0.5 V vs. Ag/AgCl) in O_2 saturated, 0.1 M H_2SO_4 (pH = 1.3) aqueous solution. The half-wave potential 0.5 V is in accordance with literature data for Cobalt-based electrodes [31]. The highest current density (J_{lim}) was achieved by the #Co2-based electrode in Figure 4C, at a potential $E = -200$ mV, $J_{\text{lim}} = 8.4$ mA cm^{-2} at 1500 rad/s. This current density was higher than the $J_{\text{lim}} = 5.57$ mA cm^{-2} achieved by the reference Pt-electrode, at 1500 rad/s, see Figure 4A. Thus, incorporation of FSP-made Co_3O_4 nanoparticles into the ORR electrode had a significant positive effect in ORR. This trend was also observed at higher rotation-speeds. Herein, for the sake of the discussion, we exemplify/compare the ORR performance values at moderate rotation speeds, i.e., 1500 rpm. The #Co3-based electrode, Figure 4D, also achieved a high ORR activity at $E = -200$ mV with a current density of $J_{\text{lim}} = 7.82$ mA cm^{-2} at 1500 rad/s. Finally, the #Co1-based electrode, Figure 4B, achieved a current density of $J_{\text{lim}} = 6.1$ mA cm^{-2} at 1500 rad/s. Comparison of #Co2 with #Co1 shows that the post-FSP calcination process had a beneficial effect on the ORR performance. In all cases, in Figure 4A–D, increased rotation speeds exerted a strong beneficial influence on current densities, a well-known phenomenon for rotating-disk-electrodes [66] as predicted by Equations (4)–(6).

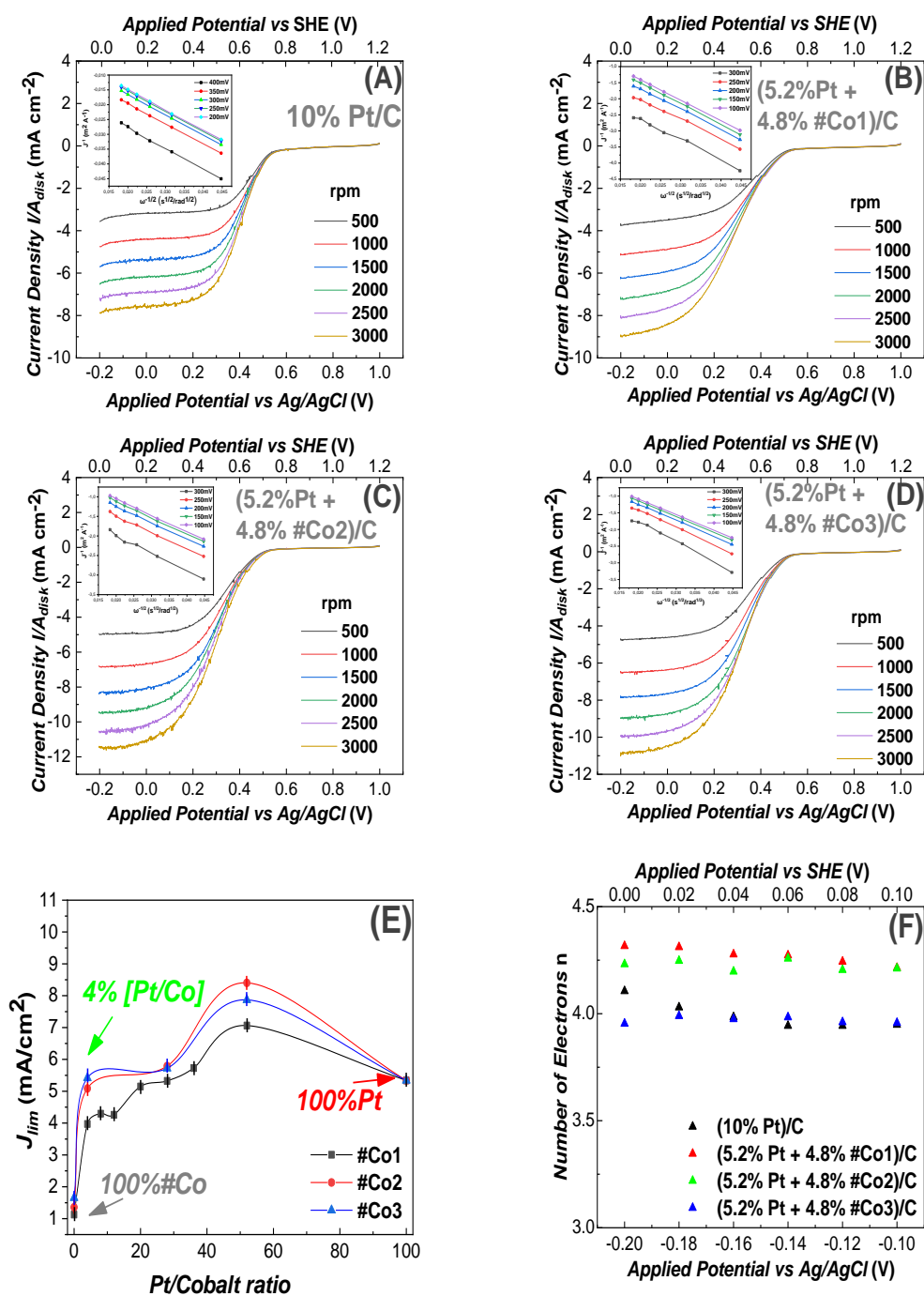


Figure 4. Linear Voltammograms for ORR, recorded using a Glassy-Carbon rotating electrode, loaded with nanocatalysts, in O₂ saturated 0.1 M H₂SO₄ solution (pH = 1.3). The potential scan rate was 10 mV/s, (A) electrode containing 10% Pt/C (reference). In (B–D) all electrodes contained (5.2% Pt 4.8% FSP-Cobalt oxide)/C. (B) #Co1-based electrode, (C) #Co2-based electrode, (D) #Co3-based electrode, (E) Limiting current density versus Pt/Cobalt ratio on the working electrodes, (F) Electron transfer number (n), estimated using Equation (6) for the data at 1500 rpm. Insets in A, B, C, D: Elovich plots J_{lim} vs. $[\text{rotation frequency}]^{-1/2}$.

The linear Elovich plots, derived using Equation (6), see inset in each frame in Figure 4, allow an estimation of the number of transferred electrons. In all cases in Figure 4, the number of transferred electrons was consistently $n \sim 4$, see Table 2. This indicates that our electrodes perform ORR via the, mostly desired, direct 4-electron process. The sigmoidal line-shape [61] of the curves in Figure 4, shows that the ORR process was diffusion-

controlled for $E < -0.1$ V, mixed-diffusion kinetic-controlled in the potential region -0.1 to 0.1 V and kinetic-controlled in the potential region 0.53 to 0.60 V [61].

Table 2. Comparison of ORR performance of the present FSP-Nanocatalysts vs. literature data for Co-based catalysts.

Catalysts on GCE (Glassy Carbon Electrodes)	Catalyst Particle Size (nm)	Medium	Catalyst Loading ($\text{mg}\cdot\text{cm}^{-2}$)	e^- Transferred	Half-Wave Potential vs SHE (V, rpm)	Catalytic Activity ($\text{mA}\cdot\text{cm}^{-2}$)	Mass Activity ($\text{A}/\text{mg}_{\text{Pt}}$)	Ref.
Co_3O_4 /rGO	12–25	Alkaline (0.1 M KOH)	0.120	3.9	0.79, 1600	12.3	-	[68]
Co_3O_4	31	Acid(BR buffer pH = 1.8)	0.643	2	0.71, 1250	0.6	-	[67]
Co_3O_4 -11	12	Alkaline (0.1 M KOH)	0.400	4	-0.052, 2400	3.5	-	[69]
CoO_x NPs/BNG	20–30	Alkaline (0.1 M KOH)	0.850	4	0.80, 1600	5.7	-	[70]
Co_3O_4 /CNTs	24–28	Alkaline (0.1 M KOH)	0.150	4	0.80, 1600	5.2	-	[71]
Co-S/G-3 (nanosheets)	26–27	Alkaline (0.1 M KOH)	0.640	4	0.75, 1600	6.6	-	[72]
Co_2O_3 @MF-C	44	Alkaline (0.1 M KOH)	0.051	4	0.85, 1600	5	-	[45]
Co-CoO@NC	15	Alkaline (0.1 M KOH)	0.100	4	0.80, 1600	4.8	-	[73]
Pt-Co Concave NCs/C	90	Acid (0.1 M HClO_4)	0.153	4	0.90, 1600	6	0.26	[74]
Pt-CoO	16	Acid (0.1 M HClO_4)	0.101	4	0.95, 1600	6.1	8.37	[75]
5.2% Pt-4.8%#Co1/Vulcan	10	Acid (0.1 M H_2SO_4)	0.041	4	0.66, 1500	6.3	0.029	this work
5.2%Pt-4.8%#Co1/ Vulcan	10	Alkaline (0.1 M NaOH)	0.041	4	0.08, 1500	5.9	0.028	this work
5.2%Pt-4.8%#Co2/Vulcan	27	Acid (0.1 M H_2SO_4)	0.041	4	0.66, 1500	8.3	0.039	this work
5.2%Pt-4.8%#Co2/ Vulcan	27	Alkaline (0.1 M NaOH)	0.041	4	0.08, 1500	8.3	0.039	this work
5.2%Pt-4.8%#Co3/Vulcan	11	Acid (0.1 M H_2SO_4)	0.041	4	0.68, 1500	7.9	0.037	this work -
5.2%Pt-4.8%#Co3/Vulcan	11	Alkaline (0.1 M NaOH)	0.041	4	0.08, 1500	7.4	0.035	this work

In Figure 4E, we compare the J_{lim} values for electrodes with different concentrations of Co-particles at 1500 rpm. We see that the highest J_{lim} current density was achieved when we used an $\sim 50:50$ Pt:Co-oxide ratio. Noticeably, our electrodes with minimal Pt of 0.4%, i.e., 9.6% #Co1 were also efficient, with an efficiency comparable to 10% Pt. The data in Figure 4E show that for a Pt-content of 5.2% (4.8% Co-oxide) the current density achieved was improved by $\sim 30\%$ vs the 10%Pt. Noticeably, at very low 0.4% Pt content, i.e., 9.6%Co-Oxide, all materials showed efficient ORR, with the best material #Co3 achieving $J_{\text{lim}} = 5.71 \text{ mA}/\text{cm}^2$. This is among the lowest Pt-contents reported so far in literature for metal-oxide nanoparticles, with common carbon-black/Vulcan as support. More specifically, to our knowledge, the best so far reported Metal-oxide with noble metal/supported on Vulcan was an electrode with 75% Pt, i.e., (7.5 wt% Pd and 2.5 wt% Co)/C, which achieved a current density of $J_{\text{lim}} = 1.8 \text{ mA}/\text{cm}^2$ at acidic pH [31]. All the present Co-based electrodes were tested for up to 50 ORR cycles in acid pH and showed practically no-change in their performance profiles.

(2) ORR at Alkaline pH: In Figure 5, we present ORR data at alkaline-pH 13.4. ORR data for the 100% Pt-based electrode as reference, are presented in Figure 5A. In all cases, the total-metal loading of each electrode was 10%. In Figure 5B–D the electrode contained 4.8%Co-oxide + 5.2% Pt, i.e., almost half of the Pt mass vs. the reference Pt-based electrode. According to Figure 5B–D all our Co-based electrodes showed the same negative ORR half-wave potential (-0.13 V vs. Ag/AgCl) This is in accordance with literature data for Cobalt-based electrodes [67] in alkaline, O_2 saturated, aqueous medium with 0.1 M NaOH (pH = 13.4). The highest current density $J_{lim} = 8.31$ mA cm^{-2} at 1500 rad/s was achieved by the #Co2-based electrode in Figure 5C, at a potential $E = -600$ mV. This current density is higher than the $J_{lim} = 5.32$ mA cm^{-2} at $E = -400$ mV, achieved by the reference Pt-electrode, at 1500 rad/s, see Figure 5A. This trend is also observed at higher rotation-speeds. The #Co3-based electrode, Figure 5D, achieved high activity at $E = -600$ mV with a limiting current density of $J_{lim} = 7.38$ mA cm^{-2} at 1500 rad/s. Finally, the #Co1-based electrode, Figure 5B, achieved a limiting current density of $J_{lim} = 4.46$ mA cm^{-2} at 1500 rad/s. Using the linear Elovich plots, see inset in each frame in Figure 5, using Equation (6), the number of transferred electrons was $n \sim 4$, see Table 2.

As in the case of acid-medium, the sigmoidal shape [61] of the curves in Figure 5, means that, in alkaline medium, the ORR process was diffusion controlled for $E < -0.55$ V, mixed diffusion kinetic controlled in the potential region from -0.05 to 0 V and kinetic-controlled in the potential region from -0.55 to -0.40 V [61].

In Figure 5E, we compare the J_{lim} values for electrodes with Pt/Co ratio at 1500 rpm. We see that in alkaline, as well in acid medium, a Co/Pt ratio $\sim 50:50$ was optimal for the ORR. Noticeably, in alkaline medium, for a Pt-content of 5.2% and 4.8% #Co3, the maximum current density was improved by 24.7% vs. the 10%Pt. At very low Pt content, i.e., 0.4% Pt + 9.6%Co-Oxide, all materials showed efficient ORR, with the best material #Co3 achieving $J_{lim} = 6.06$ mA/ cm^2 . All the present Co-based electrodes were tested for up to 50 ORR cycles in alkaline pH and showed practically no change in their performance profiles.

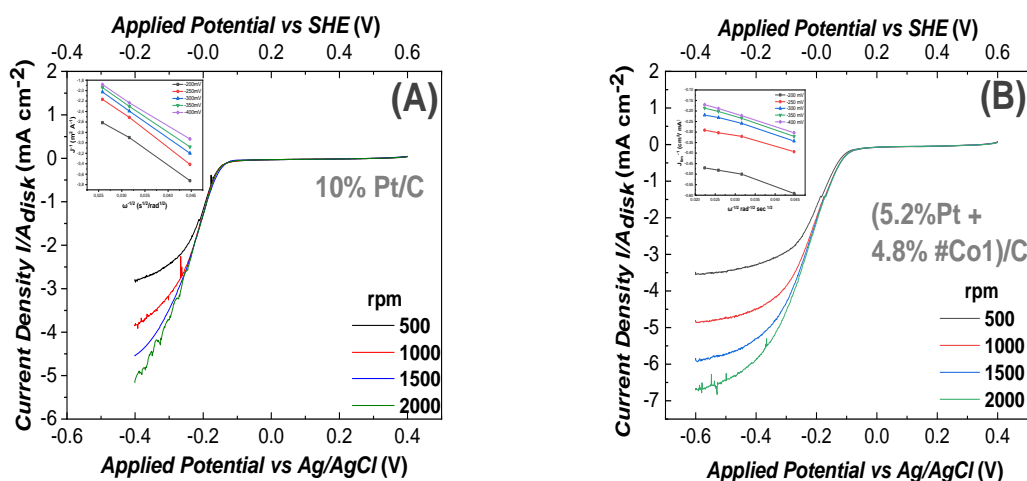


Figure 5. Cont.

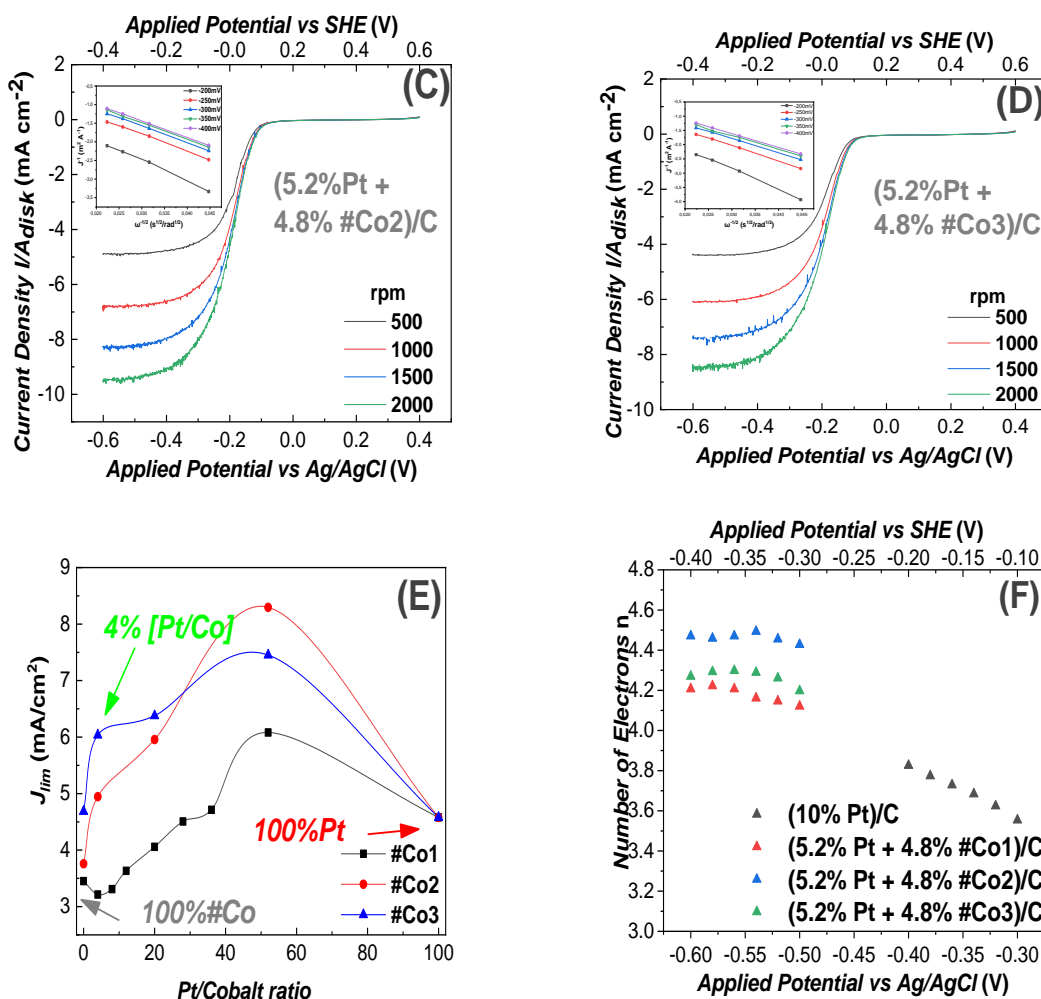


Figure 5. Linear Voltammograms for ORR, recorded using a Glassy-Carbon rotating electrode, loaded with nanocatalysts, in O_2 saturated 0.1 M NaOH solution ($pH = 13.4$). The potential scan rate was 10 mV/s, (A) electrode containing 10% Pt/C (reference). In B, C, D all electrodes contained (5.2% Pt 4.8% FSP-Cobalt oxide/C). (B) #Co1-based electrode, (C) #Co2-based electrode, (D) #Co3-based electrode, (E) Limiting current density versus Pt/Cobalt ratio on the working electrodes, (F) Electron transfer number (n), estimated using Equation (7) for the data at 1500 rpm. Insets in A, B, C, D: Elovich plots where J_{lim} vs. $[rotation\ frequency]^{-1/2}$.

3.2.2. Comparison with Literature

In Table 2, we present a comparison of ORR efficiency data, based on half wave potential and limiting current density J_{lim} ($mA \cdot cm^{-2}$) reported so far for pertinent cobalt-oxides on several supports.

According to Table 2, we can classify the ORR performances according to the pH, i.e., acid or alkaline. At alkaline pH, the best -so far reported- performance was achieved by a Co_3O_4 /rGO catalyst, that is Co_3O_4 supported on reduced Graphene-Oxide [62]. This material was reported to achieve a limiting current of $12.3 (mA \cdot cm^{-2})$ at 1600 rpm for a loading of 0.1 mg of catalyst per gr of electrode material. As analyzed by the authors [62] the reduced Graphene-Oxide played a determinative role in this ORR performance. Our best-performing electrode [5.2%Pt–4.8%#Co2/ on Vulcan carbon black] achieved a limiting current of $8.3 (mA \cdot cm^{-2})$ at 1500 rpm for a loading of 0.041 mg of catalyst per gr of electrode material. Taking into account the benefit of rGO used in [62] vs. Vulcan used in the present work, we consider that the FSP-made Co-oxide materials are highly promising for ORR. This is also evidenced by comparison of the present ORR data at alkaline pH vs. all other Co-based electrodes listed in Table 2. Concerning acid-pH, Table 2 shows that all our FSP-made catalysts supported on Vulcan, outperform all reported materials.

Co₃O₄ has the normal-spinel structure Co²⁺Co₂³⁺O₄, in which the Co³⁺ ions occupy the octahedral sites, while the Co²⁺ ions occupy the tetrahedral sites, see inset structures in Figure 1 [76]. To further peer into the Oxygen Reduction Reaction, we carried out cyclic voltammograms (CV) experiments carried in O₂ or N₂ saturated cells. The data, presented in Figures S1 and S2 of Supplementary Materials, for 5.2% + 4.8% #Co2 show a reduction peak at 136 mV, and for and 5.2% + 4.8% #Co3 at 163 mV vs Ag/AgCl. These values are consistent with the redox activity of active sites associated with cations in the higher oxidation state (Co³⁺) at the cobalt oxide surface [69]. These Co³⁺ ions would act as donor-acceptor sites, i.e., electron acceptor role due to Co₃O₄ by capturing electrons, and electron-donor properties to O₂ during oxygen reduction reaction [69]. We consider that the details of the Co-oxide nanofacets might also play a role in the ORR process. Theoretical calculation suggests that the three low Miller-index planes ({100}, {110} and {111}) of Co₃O₄ particles differ in the electronic structure, geometric bonding and chemical reactivity [77]. ORR is a surface reaction, i.e., O₂ molecules can be preferably absorbed on active surface Co²⁺ (3d⁵4s²) sites, more than on surface Co³⁺ (3d⁵4s¹) cations [71]. Our XPS analysis, revealed that in the present FSP Co₃O₄ -nanocatalysts O₂ molecules are surface-absorbed via the Pauling mode (Co . . . (O_{ads} = O)) [78]. Taking into account our XPS and CV data, we consider that the interfacial active Co²⁺ sites are able to transfer electrons on the absorbed O₂ molecules, i.e., to weaken the O-O bond and to assist breaking of O-O, while Co²⁺ is oxidized to Co³⁺ [43]. In this way, we consider that the presence Co²⁺ sites in the FSP-made materials, is of key importance for the observed ORR efficiency.

4. Conclusions

In the present work we have synthesized Co₃O₄ and CoO/Co₃O₄ nanostructures using flame spray pyrolysis (FSP). The FSP-made Co-Oxides were evaluated as electrocatalysts for ORR in acidic and alkaline medium. We have studied in detail the effect of Co-oxide/Pt ratio on ORR efficiency. We show that the FSP-made Co-oxides can perform ORR at very low-Pt loading, 0.4%. In acid medium an electrode with (5.2% Pt + 4.8% Co₃O₄), displayed the highest ORR performance ($J_{\max} = 8.31 \text{ mA/cm}^2$, $E_{1/2} = 0.66 \text{ V}$). In alkaline medium, superior performance and stability have been achieved by an electrode with (0.4% Pt + 9.6% [CoO/Co₃O₄]) with ORR activity ($J_{\max} = 3.5 \text{ mA/cm}^2$, $E_{1/2} = 0.08 \text{ V}$). XPS data suggest that Co²⁺ are promoted on the FSP-made Co-oxides and this shows a positive correlation with ORR activity. Comparison with literature shows that FSP-made Co-oxides can be considered highly promising for ORR technologies. For example, we envisage that their use with more efficient carbons supports, i.e., such as graphene or reduced graphene oxide, would further augment their efficiency. Technology-wise, the present work demonstrates that the developed FSP-protocols constitute a novel scalable process for the production of Co-oxides appropriate for oxygen reduction reaction electrodes.

Supplementary Materials: The following are available online at: <https://www.mdpi.com/article/10.3390/nano11040925/s1>, Figure S1: Cyclic Voltammetry curves of 5.2% Pt + 4.8% #Co2 at a scan rate of 20 mV s⁻¹ in a O₂ and N₂ saturated cell in 0.1 M H₂SO₄ solution, Figure S2: Cyclic Voltammetry curves of 5.2% Pt + 4.8% #Co3 at a scan rate of 20 mV s⁻¹ in a O₂ and N₂ saturated cell in 0.1 M H₂SO₄ solution.

Author Contributions: L.B. and C.M.: investigation, data curation, writing—original draft preparation. S.S.: investigation. Y.D.: conceptualization, supervision, writing—reviewing and editing. All authors have read and agreed to the published version of the manuscript.

Funding: This research received no external funding.

Data Availability Statement: Data is available upon the reasonable request from the corresponding author.

Acknowledgments: We thank Christina Papachristodoulou for assistance on the XRF analysis.

Conflicts of Interest: The authors declare no conflict of interest.

References

1. Koirala, R.; Pratsinis, S.E.; Baiker, A. Synthesis of catalytic materials in flames: Opportunities and challenges. *Chem. Soc. Rev.* **2016**, *45*, 3053–3068. [[CrossRef](#)] [[PubMed](#)]
2. Deng, C.; Wu, K.H.; Scott, J.; Zhu, S.; Amal, R.; Wang, D.W. Ternary MnO/CoMn alloy@N-doped graphitic composites derived from a bi-metallic pigment as bi-functional electrocatalysts. *J. Mater. Chem. A* **2019**, *7*, 20649–20657. [[CrossRef](#)]
3. Teoh, W.Y.; Amal, R.; Mädler, L. Flame spray pyrolysis: An enabling technology for nanoparticles design and fabrication. *Nanoscale* **2010**, *2*, 1324–1347. [[CrossRef](#)] [[PubMed](#)]
4. Mädler, L.; Kammler, H.K.; Mueller, R.; Pratsinis, S.E. Controlled synthesis of nanostructured particles by flame spray pyrolysis. *J. Aerosol Sci.* **2002**, *33*, 369–389. [[CrossRef](#)]
5. Mueller, R.; Mädler, L.; Pratsinis, S.E. Nanoparticle synthesis at high production rates by flame spray pyrolysis. *Chem. Eng. Sci.* **2003**, *58*, 1969–1976. [[CrossRef](#)]
6. Psathas, P.; Georgiou, Y.; Moularas, C.; Armatas, G.S.; Deligiannakis, Y. Controlled-Phase Synthesis of Bi₂Fe₄O₉ & BiFeO₃ by Flame Spray Pyrolysis and their evaluation as non-noble metal catalysts for efficient reduction of 4-nitrophenol. *Powder Technol.* **2020**, *368*, 268–277. [[CrossRef](#)]
7. Stacy, J.; Regmi, Y.N.; Leonard, B.; Fan, M. The recent progress and future of oxygen reduction reaction catalysis: A review. *Renew. Sustain. Energy Rev.* **2017**, *69*, 401–414. [[CrossRef](#)]
8. Ozoemena, K.I. Nanostructured platinum-free electrocatalysts in alkaline direct alcohol fuel cells: Catalyst design, principles and applications. *RSC Adv.* **2016**, *6*, 89523–89550. [[CrossRef](#)]
9. He, Q.; Cairns, E.J. Review—Recent Progress in Electrocatalysts for Oxygen Reduction Suitable for Alkaline Anion Exchange Membrane Fuel Cells. *J. Electrochem. Soc.* **2015**, *162*, F1504–F1539. [[CrossRef](#)]
10. Ma, R.; Lin, G.; Zhou, Y.; Liu, Q.; Zhang, T.; Shan, G.; Yang, M.; Wang, J. A review of oxygen reduction mechanisms for metal-free carbon-based electrocatalysts. *NPJ Comput. Mater.* **2019**, *5*, 78. [[CrossRef](#)]
11. Ramaswamy, N.; Mukerjee, S. Fundamental mechanistic understanding of electrocatalysis of oxygen reduction on Pt and non-Pt surfaces: Acid versus alkaline media. *Adv. Phys. Chem.* **2012**, *2012*, 491604. [[CrossRef](#)]
12. Wan, K.; Yu, Z.; Li, X.; Liu, M. pH Effect on Electrochemistry of Nitrogen-Doped Carbon Catalyst for Oxygen Reduction Reaction. *ACS Catal.* **2015**, *5*, 7. [[CrossRef](#)]
13. Wong, W.Y.; Daud, W.R.W.; Mohamad, A.B.; Loh, K.S. Effect of temperature on the oxygen reduction reaction kinetic at nitrogen-doped carbon nanotubes for fuel cell cathode. *Int. J. Hydrogen Energy* **2015**, *40*, 11444–11450. [[CrossRef](#)]
14. Song, C.; Zhang, J. *PEM Fuel Cell Electrocatalysts and Catalyst Layers*; Springer: London, UK, 2008; pp. 89–134. [[CrossRef](#)]
15. Gasteiger, H.A.; Kocha, S.S.; Sompalli, B.; Wagner, F.T. Activity benchmarks and requirements for Pt, Pt-alloy, and non-Pt oxygen reduction catalysts for PEMFCs. *Appl. Catal. B Environ.* **2005**, *56*, 9–35. [[CrossRef](#)]
16. Marković, N.M.; Ross, P.N. Surface science studies of model fuel cell electrocatalysts. *Surf. Sci. Rep.* **2002**, *45*, 117–229. [[CrossRef](#)]
17. Lv, H.; Li, D.; Strmcnik, D.; Paulikas, A.P.; Markovic, N.M.; Stamenkovic, V.R. Recent advances in the design of tailored nanomaterials for efficient oxygen reduction reaction. *Nano Energy* **2016**, *29*, 149–165. [[CrossRef](#)]
18. Casalongue, H.S.; Kaya, S.; Viswanathan, V.; Miller, D.J.; Friebel, D.; Hansen, H.A.; Nørskov, J.K.; Nilsson, A.; Ogasawara, H. Direct observation of the oxygenated species during oxygen reduction on a platinum fuel cell cathode. *Nat. Commun.* **2013**, *4*, 2817. [[CrossRef](#)]
19. Goswami, C.; Hazarika, K.K.; Bharali, P. Transition metal oxide nanocatalysts for oxygen reduction reaction. *Mater. Sci. Energy Technol.* **2018**, *1*, 117–128. [[CrossRef](#)]
20. Kulkarni, A.; Siahrostami, S.; Patel, A.; Nørskov, J.K. Understanding Catalytic Activity Trends in the Oxygen Reduction Reaction. *Chem. Rev.* **2018**, *118*, 2302–2312. [[CrossRef](#)]
21. Koper, M.T.M. *Fuel Cell Catalysis A Surface Science Approach*; John Wiley & Sons: Hoboken, NJ, USA, 2009; Volume 1. ISBN 9780470131169.
22. Shao, M.; Chang, Q.; Dodelet, J.P.; Chenitz, R. Recent Advances in Electrocatalysts for Oxygen Reduction Reaction. *Chem. Rev.* **2016**, *116*, 3594–3657. [[CrossRef](#)]
23. Anderson, A.B.; Roques, J.; Mukerjee, S.; Murthi, V.S.; Markovic, N.M.; Stamenkovic, V. Activation energies for oxygen reduction on platinum alloys: Theory and experiment. *J. Phys. Chem. B* **2005**, *109*, 1198–1203. [[CrossRef](#)]
24. Lim, B.; Jiang, M.; Camargo, P.H.C.; Cho, E.C.; Tao, J.; Lu, X.; Zhu, Y.; Xia, Y. Pd-Pt bimetallic nanodendrites with high activity for oxygen reduction. *Science* **2009**, *324*, 1302–1305. [[CrossRef](#)]
25. Bibi, S.; Li, P.; Zhang, J. X-Shaped donor molecules based on benzo [2,1-b: 3,4-b'] dithiophene as organic solar cell materials with PDIs as acceptors. *J. Mater. Chem. A* **2013**, *1*, 13828–13841. [[CrossRef](#)]
26. Trogadas, P.; Fuller, T.F.; Strasser, P. Carbon as catalyst and support for electrochemical energy conversion. *Carbon* **2014**, *75*, 5–42. [[CrossRef](#)]
27. Zhang, C.; Shen, X.; Pan, Y.; Peng, Z. A review of Pt-based electrocatalysts for oxygen reduction reaction. *Front. Energy* **2017**, *11*, 268–285. [[CrossRef](#)]
28. Asset, T.; Chattot, R.; Fontana, M.; Mercier-Guyon, B.; Job, N.; Dubau, L.; Maillard, F. A Review on Recent Developments and Prospects for the Oxygen Reduction Reaction on Hollow Pt-alloy Nanoparticles. *ChemPhysChem* **2018**, *19*, 1552–1567. [[CrossRef](#)]

29. Kou, R.; Shao, Y.; Wang, D.; Engelhard, M.H.; Kwak, J.H.; Wang, J.; Viswanathan, V.V.; Wang, C.; Lin, Y.; Wang, Y.; et al. Enhanced activity and stability of Pt catalysts on functionalized graphene sheets for electrocatalytic oxygen reduction. *Electrochem. Commun.* **2009**, *11*, 954–957. [[CrossRef](#)]
30. Zhan, Y.; Xie, F.; Zhang, H.; Lin, Z.; Huang, J.; Zhang, W.; Sun, X.; Zhang, Y.; Chen, J.; Meng, H. Non Noble Metal Catalyst for Oxygen Reduction Reaction and Its Characterization by Simulated Fuel Cell Test. *J. Electrochem. Soc.* **2018**, *165*, J3008–J3015. [[CrossRef](#)]
31. Bampos, G.; Bebelis, S.; Kondarides, D.I.; Verykios, X. Comparison of the Activity of Pd–M (M: Ag, Co, Cu, Fe, Ni, Zn) Bimetallic Electrocatalysts for Oxygen Reduction Reaction. *Top. Catal.* **2017**, *60*, 1260–1273. [[CrossRef](#)]
32. Zhang, Z.; Liu, J.; Gu, J.; Su, L.; Cheng, L. An overview of metal oxide materials as electrocatalysts and supports for polymer electrolyte fuel cells. *Energy Environ. Sci.* **2014**, *7*, 2535–2558. [[CrossRef](#)]
33. Liu, J.; Jiang, L.; Tang, Q.; Zhang, B.; Su, D.S.; Wang, S.; Sun, G. Coupling effect between cobalt oxides and carbon for oxygen reduction reaction. *ChemSusChem* **2012**, *5*, 2315–2318. [[CrossRef](#)] [[PubMed](#)]
34. Yu, J.; Huang, T.; Jiang, Z.; Sun, M.; Tang, C. A hybrid material combined copper oxide with graphene for an oxygen reduction reaction in an alkaline medium. *Molecules* **2019**, *24*, 441. [[CrossRef](#)] [[PubMed](#)]
35. Roche, I.; Chaînet, E.; Chatenet, M.; Vondrák, J. Carbon-supported manganese oxide nanoparticles as electrocatalysts for the Oxygen Reduction Reaction (ORR) in alkaline medium: Physical characterizations and ORR mechanism. *J. Phys. Chem. C* **2007**, *111*, 1434–1443. [[CrossRef](#)]
36. Vago, E.R.; Calvo, E.J.; Stratmann, M. Electrocatalysis of oxygen reduction at well-defined iron oxide electrodes. *Electrochim. Acta* **1994**, *39*, 1655–1659. [[CrossRef](#)]
37. Ma, L.; Zhou, H.; Xin, S.; Xiao, C.; Li, F.; Ding, S. Characterization of local electrocatalytic activity of nanosheet-structured ZnCo₂O₄/carbon nanotubes composite for oxygen reduction reaction with scanning electrochemical microscopy. *Electrochim. Acta* **2015**, *178*, 767–777. [[CrossRef](#)]
38. Huang, K.; Liu, J.; Wang, L.; Chang, G.; Wang, R.; Lei, M.; Wang, Y.; He, Y. Mixed valence CoCuMnOx spinel nanoparticles by sacrificial template method with enhanced ORR performance. *Appl. Surf. Sci.* **2019**, *487*, 1145–1151. [[CrossRef](#)]
39. Huang, W.; Zhong, H.; Li, D.; Tang, P.; Feng, Y. Reduced graphene oxide supported CoO/MnO₂ electrocatalysts from layered double hydroxides for oxygen reduction reaction. *Electrochim. Acta* **2015**, *173*, 575–580. [[CrossRef](#)]
40. Yuan, C.; Wu, H.B.; Xie, Y.; Lou, X.W. Mixed transition-metal oxides: Design, synthesis, and energy-related applications. *Angew. Chem. Int. Ed.* **2014**, *53*, 1488–1504. [[CrossRef](#)]
41. Cano, M.; Garcia-Garcia, F.J.; Rodríguez-Padrón, D.; González-Eliphe, A.R.; Giner-Casares, J.J.; Luque, R. Ultrastable Co_xSi_yO_z Nanowires by Glancing Angle Deposition with Magnetron Sputtering as Novel Electrocatalyst for Water Oxidation. *ChemCatChem* **2019**, *11*, 6111–6115. [[CrossRef](#)]
42. Shahid, M.M.; Rameshkumar, P.; Basirun, W.J.; Juan, J.C.; Huang, N.M. Cobalt oxide nanocubes interleaved reduced graphene oxide as an efficient electrocatalyst for oxygen reduction reaction in alkaline medium. *Electrochim. Acta* **2017**, *237*, 61–68. [[CrossRef](#)]
43. Xiao, J.; Kuang, Q.; Yang, S.; Xiao, F.; Wang, S.; Guo, L. Surface structure dependent electrocatalytic activity of Co₃O₄ Anchored on Graphene Sheets toward Oxygen Reduction Reaction. *Sci. Rep.* **2013**, *3*, 2300. [[CrossRef](#)] [[PubMed](#)]
44. Xie, G.; Chen, B.; Jiang, Z.; Niu, X.; Cheng, S.; Zhen, Z.; Jiang, Y.; Rong, H.; Jiang, Z.J. High catalytic activity of Co₃O₄ nanoparticles encapsulated in a graphene supported carbon matrix for oxygen reduction reaction. *RSC Adv.* **2016**, *6*, 50349–50357. [[CrossRef](#)]
45. Zhu, H.; Li, K.; Chen, M.; Wang, F. A melamine formaldehydesin route to in situ encapsulate Co₂O₃ into carbon black for enhanced oxygen reduction in alkaline media. *Int. J. Hydrogen Energy* **2017**, *42*, 25960–25968. [[CrossRef](#)]
46. Moularas, C.; Georgiou, Y.; Adamska, K.; Deligiannakis, Y. Thermoplasmonic Heat Generation Efficiency by Nonmonodisperse Core–Shell Ag₀@SiO₂ Nanoparticle Ensemble. *J. Phys. Chem. C* **2019**, *123*, 22499–22510. [[CrossRef](#)]
47. Fragou, F.; Moularas, C.; Adamska, K.; Deligiannakis, Y.; Louloudi, M. Mn(II)-Based Catalysts Supported on Nanocarbon-Coated Silica Nanoparticles for Alkene Epoxidation. *ACS Appl. Nano Mater.* **2020**, *3*, 5583–5592. [[CrossRef](#)]
48. Zsigmondy, R.; Scherrer, P. Bestimmung der inneren Struktur und der Größe von Kolloidteilchen mittels Röntgenstrahlen. *Kolloidchem. Ein Lehrb.* **1912**, *277*, 387–409. [[CrossRef](#)]
49. Sing, K. The use of nitrogen adsorption for the characterisation of porous materials. *Colloids Surfaces A Physicochem. Eng. Asp.* **2001**, *187–188*, 3–9. [[CrossRef](#)]
50. Naderi, M. Surface Area: Brunauer-Emmett-Teller (BET). In *Progress in Filtration and Separation*; Academic Press: Cambridge, MA, USA, 2014; pp. 585–608. [[CrossRef](#)]
51. Chen, Z.; Shi, E.; Li, W.; Zheng, Y.; Wu, N.; Zhong, W. Particle size comparison of hydrothermally synthesized cobalt and zinc aluminate spinels. *J. Am. Ceram. Soc.* **2002**, *85*, 2949–2955. [[CrossRef](#)]
52. Panagiotopoulou, P.; Kondarides, D.I. Effect of morphological characteristics of TiO₂-supported noble metal catalysts on their activity for the water-gas shift reaction. *J. Catal.* **2004**, *225*, 327–336. [[CrossRef](#)]
53. Molina Concha, B.; Chatenet, M. Direct oxidation of sodium borohydride on Pt, Ag and alloyed Pt-Ag electrodes in basic media. Part I: Bulk electrodes. *Electrochim. Acta* **2009**, *54*, 6119–6129. [[CrossRef](#)]
54. Van Der Vliet, D.; Wang, C.; Debe, M.; Atanasoski, R.; Markovic, N.M.; Stamenkovic, V.R. Platinum-alloy nanostructured thin film catalysts for the oxygen reduction reaction. *Electrochim. Acta* **2011**, *56*, 8695–8699. [[CrossRef](#)]

55. Mayrhofer, K.J.J.; Strmcnik, D.; Blizanac, B.B.; Stamenkovic, V.; Arenz, M.; Markovic, N.M. Measurement of oxygen reduction activities via the rotating disc electrode method: From Pt model surfaces to carbon-supported high surface area catalysts. *Electrochim. Acta* **2008**, *53*, 3181–3188. [[CrossRef](#)]
56. Spitzer, P.; Wunderli, S. *Reference Electrodes for Aqueous Solutions in Handbook of Reference Electrodes*; Springer: Berlin/Heidelberg, Germany, 2013; ISBN 9783642361883.
57. Paulus, U.A.; Schmidt, T.J.; Gasteiger, H.A.; Behm, R.J. Oxygen reduction on a high-surface area Pt/Vulcan carbon catalyst: A thin-film rotating ring-disk electrode study. *J. Electroanal. Chem.* **2001**, *495*, 134–145. [[CrossRef](#)]
58. Zhou, Y.; Guo, L.; Zhang, S.; Kaya, S.; Luo, X.; Xiang, B. Corrosion control of mild steel in 0.1 M H₂SO₄ solution by benzimidazole and its derivatives: An experimental and theoretical study. *RSC Adv.* **2017**, *7*, 23961–23969. [[CrossRef](#)]
59. Liu, J.; Jin, R.; Qiao, Y.; Wu, Y.; Wang, X.; Wang, Y. Determination of Lead(II) using glassy carbon electrode modified with hexagonal Co₃O₄ microparticles. *Int. J. Electrochem. Sci.* **2018**, *13*, 10415–10426. [[CrossRef](#)]
60. Zhao, X.Q.; Veintemillas-Verdaguer, S.; Bomati-Miguel, O.; Morales, M.P.; Xu, H.B. Thermal history dependence of the crystal structure of Co fine particles. *Phys. Rev. B Condens. Matter Mater. Phys.* **2005**, *71*, 1–7. [[CrossRef](#)]
61. Tan, Y.; Gao, Q.; Li, Z.; Tian, W.; Qian, W.; Yang, C.; Zhang, H. Unique 1D Co₃O₄ crystallized nanofibers with (220) oriented facets as high-performance lithium ion battery anode material. *Sci. Rep.* **2016**, *6*, 26460. [[CrossRef](#)]
62. Hu, S.; Melton, C.; Mukherjee, D. A facile route for the synthesis of nanostructured oxides and hydroxides of cobalt using laser ablation synthesis in solution (LASIS). *Phys. Chem. Chem. Phys.* **2014**, *16*, 24034–24044. [[CrossRef](#)] [[PubMed](#)]
63. Rivas-Murias, B.; Salgueiriño, V. Thermodynamic CoO–Co₃O₄ crossover using Raman spectroscopy in magnetic octahedron-shaped nanocrystals. *J. Raman Spectrosc.* **2017**, *48*, 837–841. [[CrossRef](#)]
64. Alex, C.; Sarma, S.C.; Peter, S.C.; John, N.S. Competing Effect of Co₃+Reducibility and Oxygen-Deficient Defects Toward High Oxygen Evolution Activity in Co₃O₄Systems in Alkaline Medium. *ACS Appl. Energy Mater.* **2020**, *3*, 5439–5447. [[CrossRef](#)]
65. Petitto, S.C.; Marsh, E.M.; Carson, G.A.; Langell, M.A. Cobalt oxide surface chemistry: The interaction of CoO(1 0 0), Co₃O₄(1 1 0) and Co₃O₄(1 1 1) with oxygen and water. *J. Mol. Catal. A Chem.* **2008**, *281*, 49–58. [[CrossRef](#)]
66. Shinozaki, K.; Zack, J.W.; Richards, R.M.; Pivovar, B.S.; Kocha, S.S. Oxygen Reduction Reaction Measurements on Platinum Electrocatalysts Utilizing Rotating Disk Electrode Technique. *J. Electrochem. Soc.* **2015**, *162*, F1144–F1158. [[CrossRef](#)]
67. Alves, I.; Santos, J.; Viégas, D.; Marques, E.; Lacerda, C.; Zhang, L.; Zhang, J.; Marques, A. Nanoparticles of Fe₂O₃ and Co₃O₄ as Efficient Electrocatalysts for Oxygen Reduction Reaction in Acid Medium. *J. Braz. Chem. Soc.* **2019**, *30*, 2681–2690. [[CrossRef](#)]
68. Liang, Y.; Li, Y.; Wang, H.; Zhou, J.; Wang, J.; Regier, T.; Dai, H. Co₃O₄ nanocrystals on graphene as a synergistic catalyst for oxygen reduction reaction. *Nat. Mater.* **2011**, *10*, 780–786. [[CrossRef](#)]
69. Xu, J.; Gao, P.; Zhao, T.S. Non-precious Co₃O₄ nano-rod electrocatalyst for oxygen reduction reaction in anion-exchange membrane fuel cells. *Energy Environ. Sci.* **2012**, *5*, 5333–5339. [[CrossRef](#)]
70. Tong, Y.; Chen, P.; Zhou, T.; Xu, K.; Chu, W.; Wu, C.; Xie, Y. A Bifunctional Hybrid Electrocatalyst for Oxygen Reduction and Evolution: Cobalt Oxide Nanoparticles Strongly Coupled to B,N-Decorated Graphene. *Angew. Chemie Int. Ed.* **2017**, *56*, 7121–7125. [[CrossRef](#)]
71. Ahmed, M.S.; Choi, B.; Kim, Y.B. Development of Highly Active Bifunctional Electrocatalyst Using Coon Carbon Nanotubes for Oxygen Reduction and Oxygen Evolution. *Sci. Rep.* **2018**, *8*, 2543. [[CrossRef](#)]
72. Odedairo, T.; Yan, X.; Ma, J.; Jiao, Y.; Yao, X.; Du, A.; Zhu, Z. Nanosheets Co₃O₄ Interleaved with Graphene for Highly Efficient Oxygen Reduction. *ACS Appl. Mater. Interfaces* **2015**, *7*, 21373–21380. [[CrossRef](#)]
73. Zhen, Z.; Jiang, Z.; Tian, X.; Zhou, L.; Deng, B.; Chen, B.; Jiang, Z.J. Core@shell structured Co-CoO@NC nanoparticles supported on nitrogen doped carbon with high catalytic activity for oxygen reduction reaction. *RSC Adv.* **2018**, *8*, 14462–14472. [[CrossRef](#)]
74. Wang, X.; Zhao, Z.; Sun, P.; Li, F. One-Step Synthesis of Supported High-Index Faceted Platinum-Cobalt Nanocatalysts for an Enhanced Oxygen Reduction Reaction. *ACS Appl. Energy Mater.* **2020**, *3*, 5077–5082. [[CrossRef](#)]
75. Sievers, G.W.; Jensen, A.W.; Quinson, J.; Zana, A.; Bizzotto, F.; Oezaslan, M.; Dworzak, A.; Kirkensgaard, J.J.K.; Smitshuysen, T.E.L.; Kadkhodazadeh, S.; et al. Self-supported Pt–CoO networks combining high specific activity with high surface area for oxygen reduction. *Nat. Mater.* **2021**, *20*, 208–213. [[CrossRef](#)] [[PubMed](#)]
76. Spencer, D.; Schroerer, D.; Hfli, C. Mossbauer study of several cobalt spinels using Co⁵⁷ and Fe⁵⁷. *Phys. Rev. B* **1974**, *9*, 3658. [[CrossRef](#)]
77. Tang, X.; Li, J.; Hao, J. Synthesis and characterization of spinel Co₃O₄ octahedra enclosed by the {1 1 1} facets. *Mater. Res. Bull.* **2008**, *43*, 2912–2918. [[CrossRef](#)]
78. Yeager, E. Dioxygen electrocatalysis: Mechanisms in relation to catalyst structure. *J. Mol. Catal.* **1986**, *38*, 5–25. [[CrossRef](#)]